PENN INSTITUTE for ECONOMIC RESEARCH
UNIVERSITY of PENNSYLVANIA

The Ronald O. Perelman Center for Political Science and Economics (PCPSE)
133 South 36th Street
Philadelphia, PA 19104-6297

pier@econ.upenn.edu
http://economics.sas.upenn.edu/pier

PIER Working Paper
20-012

Optimal Combination of Arctic Sea Ice Extent Measures: A Dynamic Factor Modeling Approach

FRANCIS X. DIEBOLD
University of Pennsylvania

MAXIMILIAN GOBEL
ISEG - Universidade de Lisboa

PHILIPPE GOULET COULOMBE
University of Pennsylvania

GLENN D. RUDEBUSCH
Federal Reserve Bank of San Francisco

BOYUAN ZHANG
University of Pennsylvania

March 31, 2020

https://ssrn.com/abstract=3566029

Optimal Combination of Arctic Sea Ice Extent Measures: A Dynamic Factor Modeling Approach

Francis X. Diebold
University of Pennsylvania

Maximilian Göbel
ISEG - Universidade de Lisboa

Philippe Goulet Coulombe
University of Pennsylvania

Glenn D. Rudebusch
Federal Reserve Bank of San Francisco

Boyuan Zhang
University of Pennsylvania

March 31, 2020

Abstract: The diminishing extent of Arctic sea ice is a key indicator of climate change as well as an accelerant for future global warming. Since 1978, Arctic sea ice has been measured using satellite-based microwave sensing; however, different measures of Arctic sea ice extent have been made available based on differing algorithmic transformations of the raw satellite data. We propose and estimate a dynamic factor model that combines four of these measures in an optimal way that accounts for their differing volatility and cross-correlations. From this model, we extract an optimal combined measure of Arctic sea ice extent using the Kalman smoother.

Acknowledgments: For comments and/or assistance we thank Preston Ching, Akshay Malhotra, Gladys Teng, David Wigglesworth, Samantha Wu-Georges, Kan Xu, and the Penn Climate Econometrics Research Group. The views expressed herein are those of the authors and do not necessarily represent those of others in the Federal Reserve System.

Key words: Climate modeling, nowcasting, model averaging, ensemble averaging

JEL codes: Q54, C22

Contact: fdiebold@sas.upenn.edu

1 Introduction

Climate change is among the most pressing issues of our time, with many severe economic, environmental, and geopolitical consequences. Recently, the application of time series analytical methods to this topic – and, more broadly, a "climate econometrics" – has emerged as a vibrant research literature, as highlighted, for example, in Hillebrand et al. (2020) and the references therein. One important issue that these methods can address is the diminishing area or extent of Arctic sea ice. The loss of Arctic sea ice is a vital focus point of climate study because it is both an ongoing conspicuous *effect* of climate change and a *cause* of additional climate change via feedback loops, including the fact that reduced Arctic sea ice boosts solar energy absorption (Diebold and Rudebusch, 2019).

There are, however, several alternative measures of Arctic sea ice extent based on different processing methodologies of the underlying satellite-based microwave measurement data, and the choice among these measures is not clear-cut (Bunzel et al., 2016). In this paper, we study four such sea ice extent (*SIE*) measures, which we denote as Sea Ice Index (SIE^S), Goddard Bootstrap (SIE^G), JAXA (SIE^J), and Bremen (SIE^B). The top panel of Figure 1 provides time series plots of these four measures of Arctic *SIE* for the satellite measurement era, which started in 1978. The four measures appear almost identical, because their scale is dominated by large seasonal swings. However, the effects of seasonality can be removed by plotting each month separately for the four series, as done in the lower twelve panels of Figure 1. Of course, the Arctic *SIE* measures all trend down in every month, with steeper trends for the summer months (e.g., August, September, October). (Note the different axis scales for different months.) There are also systematic differences across indicators. SIE^G, for example, tends to be high, and SIE^J tends to be low, while SIE^S and SIE^B are intermediate. But the deviations between various pairs of measures are not rigid; that is, they are not simply parallel translations of each other. Instead there are sizable time-varying differences among the various measures.

All of this suggests treating the various measures as noisy "indicators" of a latent true sea ice extent, which in turn suggests the possibility of blending them into a single combined indicator with less measurement error. Indeed some prominent studies have used simple equally-weighted averages of competing indicators, with precisely that goal. For example, a recent report on the state of the cryosphere (IPCC, 2019) uses a simple average of three indicators.[1] Simple averages, however, are often sub-optimal. Optimality generally requires use of *weighted* averages giving, for example, less weight to noisier indicators. Motivated by these considerations, in this paper,

[1] See the notes for Figure 3.3, page 3-13.

we propose and explore a dynamic factor state-space model that combines the various published measures into an optimal measure of sea ice extent, which we extract using the Kalman smoother.

We proceed as follows. In section 2, we describe the four leading Arctic sea ice extent indicators that we study, and the satellites, sensors, and algorithms used to produce them. In section 3, we propose a basic dynamic-factor state-space model for sea ice extent and use it to obtain optimal extractions of latent extent. We conclude in section 4.

2 Four Arctic Sea Ice Extent Indicators

Sea ice extent (*SIE*) indicators are constructed from satellite measurements of the earth's surface using passive microwave sensing, which is unaffected by cloud cover or a lack of sunlight. Several steps are necessary to convert raw reflectivity observations into final *SIE* measurements. First, for a polar region divided into a grid of individual cells, various sensors record a brightness reading or "brightness temperature" for each cell. An algorithm then transforms these brightness readings into fractional surface coverage estimates – sea ice concentration (*SIC*) values – for each grid cell. Finally, *SIE* is calculated by summing the area of all cells with at least 15 percent ice surface coverage.[2] This up-rounding in *SIE* is effectively a bias correction, as determining the edge between ice and water can be especially difficult in the summer, when, for example, melting pools on summer ice surfaces can be mistaken for ice-free open water (Meier and Stewart, 2019).

Different algorithms for processing the raw measurements importantly shape the final *SIE* estimates. In addition, the *SIE* seiries are based on raw data that can be obtained from somewhat different satellites and sensors (Comiso et al. (2017), Comiso (2007)). In this section, we review some aspects of the satellites, sensors, and algorithms that underlie the *SIE* measures.

2.1 Satellites and Sensors

Table 1 summarizes the operative dates of the various satellites and sensors relevant for Arctic ice measurement. The first multi-frequency sensor equipped on a satellite was the Scanning Multichannel Microwave Radiometer (SMMR) launched in 1978 (Cavalieri et al., 1996). Starting in 1987, later sensors – the Special Sensor Microwave Imager (SSM/I) and the Special Sensor Microwave Imager/Sounder (SSMIS) – offered higher resolution images.[3] In 2002 and 2012, respectively, the Advanced Microwave Scanner Radiometer for EOS (AMSR-E) and Advanced

[2] Parkinson and Cavalieri (2008) discusses reasons for using a 15 percent cutoff.

[3] For detailed discussion of sensor characteristics see `https://nsidc.org/ancillary-pages/smmr-ssmi-ssmis-sensors`.

Figure 1: Four Sea Ice Extent Indicators

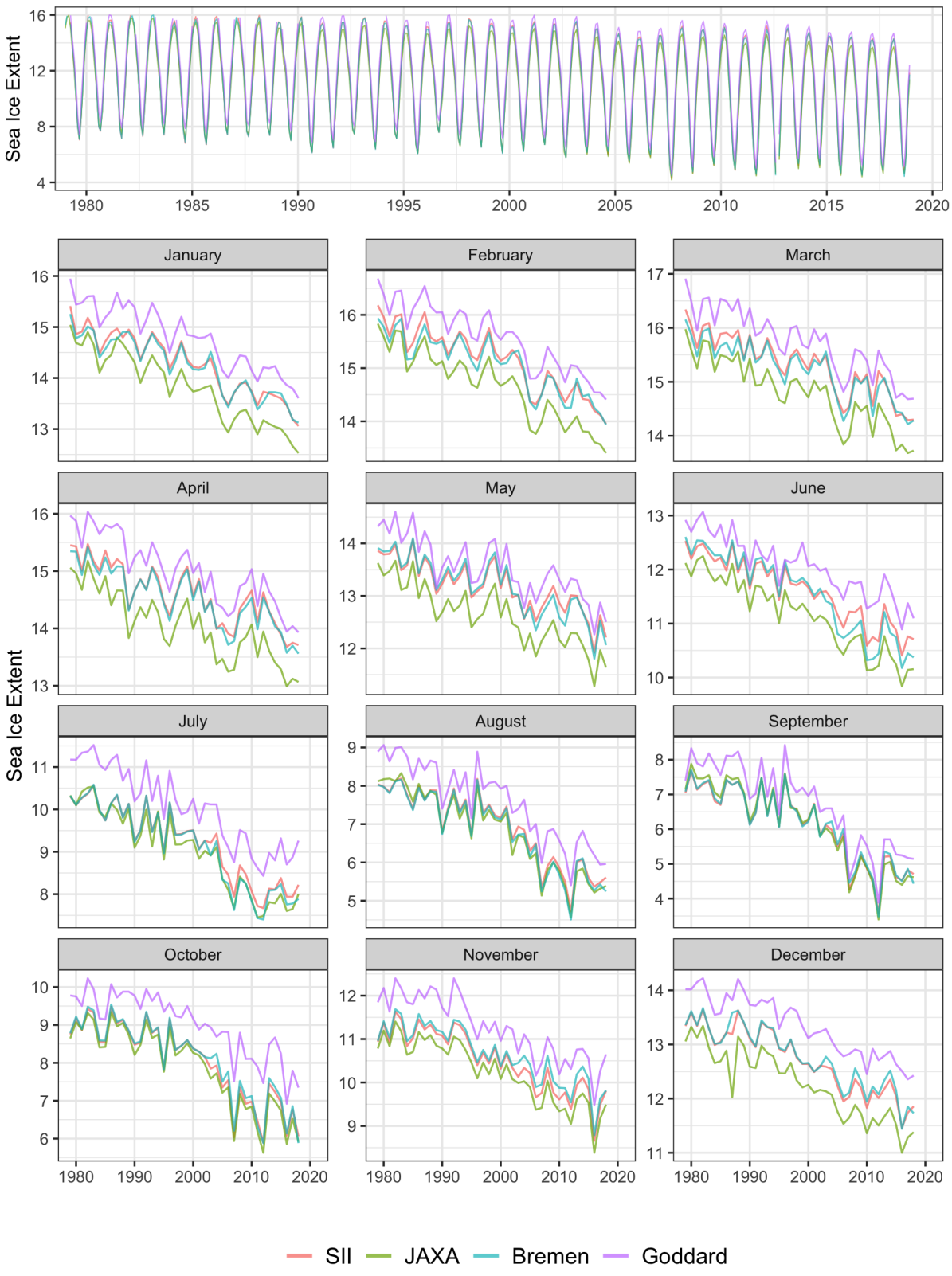

Notes: We show the Sea Ice Index (SII), Japan Aerospace Exploration agency (JAXA), University of Bremen (Bremen), and Goddard Bootstrap (Goddard). Units are millions of square kilometers.

Table 1: Satellites, Sensors, and Algorithms

Satellite / Sensor	NASA Team		Goddard Bootstrap		JAXA Bootstrap		ASI	
	Start	End	Start	End	Start	End	Start	End
Nimbus-7 SMMR	10/26/1978	08/20/1987	11/01/1978	07/31/1987	11/1978	07/1987	1972	...
DMSP-F8 SSM/I	08/21/1987	12/18/1991	08/01/1987	12/17/1991	07/1987	...	...	...
DMSP-F11 SSM/I	12/19/1991	09/29/1995	12/18/1991	05/09/1995	...	...	...	...
DMSP-F13 SSM/I	09/30/1995	12/31/2007	05/10/1995	12/31/2007	...	06/2002	...	12/2010
DMSP-F17 SSMIS	01/01/2008	12/31/2017	01/01/2008	present			10/2011	07/2012
DMSP-F18 SSMIS	01/01/2018	present						
EOS/Aqua AMSR-E					06/2002	10/2011	2003	10/2011
Coriolis WindSat					10/2011	07/2012		
GCOM-W1 AMSR2					07/2012	present	07/2012	present

Notes: NASA Team and Goddard Bootstrap dates from Fetterer et al. (2017). JAXA Bootstrap dates from `https://kuroshio.eorc.jaxa.jp/JASMES/climate/index.html`. ASI dates from `https://seaice.uni-bremen.de/sea-ice-concentration/time-series/`.

Microwave Scanner Radiometer 2 (AMSR2) sensors were launched and provided further improvements in resolution (Comiso et al., 2017).[4] Given the inclinations of the satellite orbits and the spherical shape of the earth, all of the satellites share an inability to observe the Arctic *pole hole* – a circular region at the very top of the world. The size of the pole hole varies across sensors, but historically, there is full confidence that it fulfills the 15 percent *SIC* requirement (Meier and Stewart, 2019).

Table 1 also describe the underlying source data for our four *SIE* indicators. These measures use algorithms to transform the raw satellite brightness data into *SIC* and *SIE* values. We now turn to a more detailed discussion of these algorithms to illuminate the differences across *SIE* indicators.

2.2 From Raw Measurement to *SIE*: Algorithmic Transformations

Once brightness data have been recorded by satellite sensors, an algorithm converts the measurements into estimates of *SIC*. Here, we discuss the algorithms and other details of the various *SIE* indicators.

2.2.1 Sea Ice Index

Updated on a daily basis and distributed by the *National Snow & Ice Data Center* (NSIDC), the Sea Ice Index (SII or SIE^S) combines two separate Sea Ice indicators: (1) the Sea Ice Concentrations from Nimbus-7 SMMR and DMSP SSM/I-SSMIS Passive Microwave Data (NASA Team)

[4]Early in the sample, operational problems prevented data delivery for several days during 1986 and between December 1987 and January 1988 (Comiso, 2017). For more recent technical difficulties, see `https://www.nrl.navy.mil/WindSat/Description.php`.

(Cavalieri et al., 1996) – produced at the *Goddard Space Flight Center* – and (2) the Near-Real-Time DMSP SSMIS Daily Polar Gridded Sea Ice Concentrations (NRTSI) (Maslanik and Stroeve, 1999) – produced by the NSIDC itself.[5] A time-lag of about one year between the *SIE* estimates by NASA Team and its publication in the NSIDC database requires the NRTSI to complement the SII.

The NRTSI follows the NASA Team algorithm as closely as possible, but inconsistencies between the two series cannot be ruled out entirely (Fetterer et al., 2017). In particular, the two sub-indicators use brightness temperatures from different providers.[6] These raw readings can be distorted by weather effects, making open water look like sea ice cover. Therefore, post-calculation quality checks apply land and ocean masks, to remove errorneous and implausible ice covers. However, NASA Team and NRTSI do not apply the exact same filters (Fetterer et al., 2017). The former algorithm additionally screens the data manually for falsely detected ice formation (Cavalieri et al., 1996), which can enhance accuracy but also reduce transparency of the final measurements.

As Table 1 shows, the SII obtains the raw data from different generations of satellites and sensors. To make the data comparable, a linear least-squares model on the brightness temperatures, as reported by the two distinct sensors for an overlapping period of operation, is intended to adjust the reference points of 100 percent sea ice and 100 percent open water. These *tie points* then remain fixed over the lifetime of the new system (Cavalieri et al., 2012).

2.2.2 Goddard Bootstrap

Another sea ice indicator, distributed by the NSIDC, relies on *SIC* estimates of the Goddard Bootstrap algorithm (SIE^G).[7] Despite the NASA Team and the Goddard Bootstrap algorithms having both been developed at the *NASA Goddard Space Flight Center*, there are some differences between the two approaches. These arise mostly from the calibration of tie points: Other than the NASA Team, which adjusts these reference points for 100 percent open water and 100 percent ice only when a new satellite or sensor becomes operational, the Goddard Bootstrap algorithm adjusts these reference points on a daily basis to account for varying weather conditions (Comiso et al., 2017). Differing weather filters, and sensitivities to varying physical temperature also lead to differences in the final measurements(Comiso et al., 1997). In contrast to the NASA Team, the

[5] See `https://doi.org/10.7265/N5K072F8`.

[6] Maslanik and Stroeve (1999) takes the data from the National Oceanic and Atmospheric Administration Comprehensive Large Array-data Stewardship System (NOAA CLASS); (Cavalieri et al., 1996) uses data processed at the NASA Goddard Space Flight Center.

[7] For detailed algorithm description see Comiso et al. (2017b). For the data, see `https://doi.org/10.5067/7Q8HCCWS4I0R`.

strength of the Goddard Bootstrap algorithm is the identification of melting sea ice. Therefore, the Goddard Bootstrap algorithm provides more accurate estimates of the edge of the ice cover (Goldstein et al., 2018).

Although differences between SIE^S and SIE^G are generally assessed to be small, they cannot necessarily be neglected (Goldstein et al., 2018). The differences between the NASA Team and Goddard Bootstrap algorithms occur especially during the melting season, when the former generally reports larger deviations from ship or radar observations. However, the relative accuracy of the two algorithms is not clear-cut, as the Goddard Bootstrap algorithm is highly sensitive to physical temperature and underestimates *SIC* during winter times in the higher latitudes of the Arctic region.

2.2.3 Japan Aerospace Exploration Agency

As listed in Table 1, both SIE^S and SIE^G rely on the same set of instruments, which have been criticized for their low spatial resolution (Goldstein et al., 2018). The Japan Aerospace Exploration Agency (JAXA) sea ice measure (SIE^J) uses an adapted version of the Goddard Bootstrap algorithm to derive *SIC* measures from satellite readings with higher spatial resolution (Comiso et al., 2017b) .[8] However, readings from these high resolution satellites are only available since 2000, so their data must merged with observations from older sensors to extend the data coverage to 1978 (Comiso et al., 2017). SIE^J also distinguishes itself from SIE^S and SIE^G by using a moving average of five days of observation to compensate for potentially missing data.

2.2.4 University of Bremen

Using observations delivered by the high-resolution AMSR-E sensor, a group of researchers at the University of Bremen developed the ARTIST Sea Ice (ASI) algorithm (Spreen et al., 2008) to estimate daily *SIC*.[9] The time-series (SIE^B) uses different algorithms for different sensors. Until the launch of the AMSR-E sensor in 2003, SIE^B used the NASA Team algorithm to transform brightness readings into *SIC* values. From then on, the NASA Team algorithm is replaced by the ASI.[10]

[8] For description and data see `https://kuroshio.eorc.jaxa.jp/JASMES/climate/index.html`.

[9] Monthly data from `https://seaice.uni-bremen.de/data/amsr2/today/extent_n_19720101-20181231_amsr2.txt`.

[10] See `https://seaice.uni-bremen.de/sea-ice-concentration-amsr-eamsr2/time-series/`.

3 Optimal Extraction of Latent Extent

The four sea ice measures discussed above differ in terms of the raw data sources and the algorithms used to process those data. They can be viewed as distinct indicators of an unobserved or latent "true" sea ice extent, SIE^*, and blending such a set of noisy indicators into a composite can produce a single series with less measurement error. Here we formalize this intuition in a state-space dynamic-factor model, from which we extract an optimal composite estimate of SIE^* from the four component indicators.

3.1 A Dynamic Factor Model

We work in a state-space environment, modeling each of the four indicators (SIE^S, SIE^J, SIE^B, and SIE^G) as driven by latent true sea ice extent, SIE^*, with an additive measurement error.[11]

The measurement equation is

$$\begin{pmatrix} SIE_t^S \\ SIE_t^J \\ SIE_t^B \\ SIE_t^G \end{pmatrix} = \begin{pmatrix} \lambda_S \\ \lambda_J \\ \lambda_B \\ \lambda_G \end{pmatrix} SIE_t^* + \begin{pmatrix} \varepsilon_t^S \\ \varepsilon_t^J \\ \varepsilon_t^B \\ \varepsilon_t^G \end{pmatrix}, \tag{1}$$

where

$$\varepsilon_t = (\varepsilon_t^S, \varepsilon_t^J, \varepsilon_t^B, \varepsilon_t^G)' \sim iid\, N(0, \Sigma), \tag{2}$$

with

$$\Sigma = \begin{pmatrix} \sigma_{SS}^2 & \cdot & \cdot & \cdot \\ \sigma_{JS}^2 & \sigma_{JJ}^2 & \cdot & \cdot \\ \sigma_{BS}^2 & \sigma_{BJ}^2 & \sigma_{BB}^2 & \cdot \\ \sigma_{GS}^2 & \sigma_{GJ}^2 & \sigma_{GB}^2 & \sigma_{GG}^2 \end{pmatrix}. \tag{3}$$

The transition equation is

$$SIE_t^* = \rho\, SIE_{t-1}^* + TREND_t + SEASONAL_t + \eta_t, \tag{4}$$

where $\eta_t \sim iidN(0, \sigma_{\eta\eta}^2)$ is orthogonal to ε_t at all leads and lags. Various modeling approaches are distinguished by their treatment of $TREND_t$ and $SEASONAL_t$. We follow Diebold and Rudebusch (2019) and allow for 12 monthly deterministic seasonal effects, each of which is endowed with

[11] The approach parallels Aruoba et al. (2016), who extract latent U.S. GDP from noisy expenditure-side and income-side estimates.

(possible) deterministic quadratic trend.[12] This results in a blended deterministic "trend/seasonal" given by

$$TREND_t + SEASONAL_t = \sum_{i=1}^{12} a_i D_{it} + \sum_{j=1}^{12} b_j D_{jt} \cdot TIME_t + \sum_{k=1}^{12} c_k D_{kt} \cdot TIME_t^2, \tag{5}$$

where D_i indicates month i and $TIME$ indicates time. Hence the full transition equation is

$$SIE_t^* = \rho SIE_{t-1}^* + \sum_{i=1}^{12} a_i D_{it} + \sum_{j=1}^{12} b_j D_{jt} \cdot TIME_t + \sum_{k=1}^{12} c_k D_{kt} \cdot TIME_t^2 + \eta_t. \tag{6}$$

The model is already in state-space form, and one pass of the Kalman filter, initialized with the unconditional state mean and covariance matrix, provides the 1-step prediction errors necessary to construct the Gaussian likelihood. We maximize the likelihood using the EM algorithm and calculate standard errors from the analytic Hessian matrix. Following estimation, we use the Kalman smoother to obtain the minimum variance unbiased extraction of SIE^* from the estimated model. The smoother averages across indicators, but it desirably produces optimally weighted averages rather than simple averages. The smoother also averages over time, using data both before and after time t to estimate SIE_t^*, which is also necessary for minimum-variance extraction, due to the serial correlation in SIE^*. For details see Harvey (1989).

One or more restrictions are necessary for identification. The standard approach is to normalize a factor loading, which amounts to an unbiasedness assumption. Normalizing λ_S=1, for example, amounts to an assumption that SIE^S is unbiased for SIE^*. Whether there truly exists such an unbiased indicator (and if so, which) is of course an open question – one can never know for sure. SIE^S and SIE^G are the most widely used indicators (Meier et al. (2014), Peng et al. (2013)), so it is natural to consider normalizing on λ_S or λ_G. We explore both.

3.2 Estimated Measurement Equation

The estimated measurement equation (1), normalized with λ_S=1, is

[12] Alternatively, one could entertain stochastic trend and seasonality, but we leave that to future research. A simple approach would be separate month-by month modeling so that there is no seasonality, whether with one unit root, as in (for month m) $TREND_{m,t} = d_m + TREND_{m,t-1} + u_{m,t}$, or two unit roots, as in $TREND_{m,t} = d_{mt} + TREND_{m,t-1} + u_{m,t}$, where $d_{m,t} = d_{m,t-1} + v_{m,t}$.

$$\begin{pmatrix} SIE_t^S \\ SIE_t^J \\ SIE_t^B \\ SIE_t^G \end{pmatrix} = \begin{pmatrix} 1 \\ \underset{[0.0006]}{0.968} \\ \underset{[0.0005]}{0.998} \\ \underset{[0.0013]}{1.045} \end{pmatrix} SIE_t^* + \begin{pmatrix} \varepsilon_t^S \\ \varepsilon_t^J \\ \varepsilon_t^B \\ \varepsilon_t^G \end{pmatrix}, \tag{7}$$

where standard errors appear beneath each estimated loading. All indicators are estimated to load heavily on SIE^*, with all $\hat{\lambda}'s$ very close to 1. SIE^J loads least heavily ($\hat{\lambda_J}$=0.968), in accord with its generally lower values in Figure 1, and SIE^G loads most heavily ($\hat{\lambda_G}$=1.045), in accord with its generally higher values. SIE^B loads with an estimated coefficient insignificantly different from 1, and, of course, the SIE^S loading is 1 by construction. Hence, the estimation results accord with Figure 1, with SIE^S and SIE^B more in the center of the range and SIE^J and SIE^G more extreme.

Alternatively, the estimated measurement equation normalized with λ_G=1 is

$$\begin{pmatrix} SIE_t^S \\ SIE_t^J \\ SIE_t^B \\ SIE_t^G \end{pmatrix} = \begin{pmatrix} \underset{[0.0012]}{0.956} \\ \underset{[0.0010]}{0.926} \\ \underset{[0.0012]}{0.955} \\ 1 \end{pmatrix} SIE_t^* + \begin{pmatrix} \varepsilon_t^S \\ \varepsilon_t^J \\ \varepsilon_t^B \\ \varepsilon_t^G \end{pmatrix} \tag{8}$$

The estimated loadings in equations (7) and (8), corresponding to λ_S=1 and λ_G=1 respectively, are the same up to the normalization. All estimated loadings are now less than one, because we now normalize on Goddard, which is always the highest.

Now consider the associated measurement error covariance matrix (3). The estimate for the λ_S=1 normalization is

$$\hat{\Sigma} = \begin{pmatrix} \underset{[0.004]}{0.007} & \cdot & \cdot & \cdot \\ \underset{[0.004]}{-0.001} & \underset{[0.005]}{0.018} & \cdot & \cdot \\ \underset{[0.004]}{0.004} & \underset{[0.004]}{-0.001} & \underset{[0.005]}{0.015} & \cdot \\ \underset{[0.005]}{-0.021} & \underset{[0.005]}{-0.002} & \underset{[0.005]}{-0.018} & \underset{[0.008]}{0.069} \end{pmatrix}. \tag{9}$$

with implied estimated correlation matrix

$$\hat{R} = \begin{pmatrix} 1 & \cdot & \cdot & \cdot \\ -0.066 & 1 & \cdot & \cdot \\ 0.397 & -0.089 & 1 & \cdot \\ -0.964 & -0.045 & -0.566 & 1 \end{pmatrix}. \tag{10}$$

Note that $\hat{\sigma}^2_{GG}$ is much higher than any of $\hat{\sigma}^2_{SS}$, $\hat{\sigma}^2_{JJ}$, and $\hat{\sigma}^2_{BB}$, potentially due to different indicators using different methods to determine tie points, i.e., reference points of brightness for 100% sea ice and 100% open water. The choice is crucial for accurate measurement of *SIC* within grid cells. Tie points, moreover, need not be constant, as brightness readings are sensitive to weather effects and atmospheric forcings (Ivanova et al., 2015). Dynamic tie-point calibration is potentially desirable because it can decrease the bias of *SIC* measurements (Comiso et al., 2017). The latest version of the Goddard Bootstrap algorithm, in particular, calibrates tie points daily. One would expect, however, that the bias reduction from dynamic tie-point calibration may come at the cost of potential discontinuities that increase measurement error variance. Our results confirm that conjecture. Our estimate of $\hat{\sigma}^2_{GG}$ is about 4.5 times that of $\hat{\sigma}^2_{BB}$ (which uses constant tie points).

Alternatively, the estimated measurement error covariance matrix for the λ_G=1 normalization is

$$\hat{\Sigma} = \begin{pmatrix} \underset{[0.004]}{0.007} & \cdot & \cdot & \cdot \\ \underset{[0.004]}{-0.001} & \underset{[0.004]}{0.017} & \cdot & \cdot \\ \underset{[0.004]}{0.004} & \underset{[0.004]}{-0.002} & \underset{[0.005]}{0.015} & \cdot \\ \underset{[0.005]}{-0.021} & \underset{[0.005]}{-0.002} & \underset{[0.005]}{-0.019} & \underset{[0.009]}{0.068} \end{pmatrix}. \tag{11}$$

with implied estimated correlation matrix

$$\hat{R} = \begin{pmatrix} 1 & \cdot & \cdot & \cdot \\ -0.077 & 1.000 & \cdot & \cdot \\ 0.395 & -0.105 & 1.000 & \cdot \\ -0.957 & -0.054 & -0.573 & 1.000 \end{pmatrix}. \tag{12}$$

Table 2: Trend/Seasonal Parameter Estimates

	λ_S=1			λ_G=1		
	a_i	b_j	c_k	a_i	b_j	c_k
Jan	5.154 [0.578]	1.356 [0.994]	−4.707 [2.002]	5.200 [0.603]	0.636 [1.019]	−3.401 [2.068]
Feb	5.137 [0.626]	−0.292 [0.984]	−1.679 [2.007]	5.051 [0.659]	−0.254 [1.017]	−1.683 [2.073]
Mar	4.714 [0.658]	−1.222 [0.986]	0.974 [2.009]	4.592 [0.694]	−1.236 [1.019]	1.104 [2.075]
Apr	3.945 [0.664]	−1.791 [0.992]	2.165 [2.003]	3.785 [0.700]	−1.823 [1.025]	2.308 [2.069]
May	2.881 [0.638]	0.139 [1.001]	−1.896 [2.003]	2.688 [0.672]	0.216 [1.035]	−2.001 [2.069]
Jun	2.628 [0.575]	−1.206 [1.000]	−1.225 [2.005]	2.455 [0.606]	−1.206 [1.033]	−1.275 [2.071]
Jul	1.707 [0.521]	−2.012 [1.004]	−2.099 [2.006]	1.522 [0.549]	−2.058 [1.037]	−2.117 [2.073]
Aug	0.680 [0.447]	0.428 [1.018]	−5.414 [2.011]	0.488 [0.471]	0.523 [1.053]	−5.565 [2.077]
Sep	1.675 [0.354]	−0.736 [1.015]	−3.508 [2.033]	1.578 [0.373]	−0.708 [1.049]	−3.518 [2.101]
Oct	3.838 [0.327]	1.587 [1.015]	−5.825 [2.037]	3.851 [0.344]	1.722 [1.048]	−5.913 [2.105]
Nov	4.929 [0.392]	−2.026 [1.012]	4.177 [2.065]	4.958 [0.413]	−2.115 [1.046]	4.638 [2.135]
Dec	5.362 [0.483]	−0.714 [1.02]	0.014 [2.011]	5.363 [0.509]	−0.709 [1.054]	0.124 [2.077]

Notes: The b_j are $\times 10^3$ and the c_k are $\times 10^6$.

3.3 Estimated Transition Equation

Now let us move to the transition equation (6). Using the λ_S=1 normalization we obtain $\hat{\rho}$=0.712 [0.041] and trend/seasonal parameter estimates ($\hat{a}_i$, $\hat{b}_j$, and $\hat{c}_k$) as reported in the λ_S=1 columns of Table 2. Trends for all months are highly significant and downward sloping. The trends for summer months (August, September, October, November) display a notable negative, and generally statistically significant, curvature, whereas for non-summer months, the quadratic trend terms are generally small and statistically insignificant. For the λ_G=1 normalization we get $\hat{\rho}$=0.732 [0.041] and trend/seasonal parameter estimates ($\hat{a}_i$, $\hat{b}_j$, and $\hat{c}_k$) as reported in the λ_G=1 columns of Table 2. The λ_S=1 and λ_G=1 results are very similar.

3.4 Extracted Latent Sea Ice Extent

In Figures 2 (λ_S=1) and 3 (λ_G=1) we show we show optimal latent sea ice extent extractions ($\widehat{SIE}^*$) in black, together with the four raw indicators in color, by month. First consider Figure 2. Of course $\widehat{SIE}^*(\lambda_S{=}1)$ is centered on SIE^S due to the λ_S=1 normalization. Moreover, $\widehat{SIE}^*(\lambda_S{=}1)$ is always very close – almost identical – to SIE^S (and close to SIE^B, because SIE^B tends to be very close to SIE^S).

Now consider Figure 3 (λ_G=1). Due to the different normalization, $\widehat{SIE}^*(\lambda_G{=}1)$ is centered not on SIE^S but rather on SIE^G, so $\widehat{SIE}^*(\lambda_G{=}1)$ is shifted upward relative to $\widehat{SIE}^*(\lambda_S{=}1)$. The location of $\widehat{SIE}^*(\lambda_G{=}1)$ relative to SIE^G, moreover, clearly varies by month. In winter months, it tends to be greater than SIE^G, whereas in summer months it tends to be less than SIE^G. Note in particular that the variation of $\widehat{SIE}^*(\lambda_G{=}1)$ around SIE^G is noticeably greater than the variation of $\widehat{SIE}^*(\lambda_S{=}1)$ around SIE^S. Clearly $\widehat{SIE}^*(\lambda_G{=}1)$ is influenced more by movements in other indicators (SIE^S, SIE^J, and SIE^B) than is $\widehat{SIE}^*(\lambda_S{=}1)$.

The fact that $\widehat{SIE}^*(\lambda_S{=}1)$ and $\widehat{SIE}^*(\lambda_G{=}1)$ are different, both in terms of level and variation around the level, limits their usefulness for research focusing on level, as the level depends entirely on identifying assumptions. However, and crucially, in an important sense $\widehat{SIE}^*(\lambda_S{=}1)$ and $\widehat{SIE}^*(\lambda_G{=}1)$ are highly similar: *The model and identification scheme makes* $\widehat{SIE}^*(\lambda_S{=}1)$ *and* $\widehat{SIE}^*(\lambda_G{=}1)$ *identical up to a linear transformation.* This is clear in Figure 4, which plots the two competing extracted factors, month-by-month. Regressions of $\widehat{SIE}^*(\lambda_G{=}1)$ on $\widehat{SIE}^*(\lambda_S{=}1)$ yield highly-significant intercepts not far from zero, highly-significant slopes near 1.0, and R^2 values above 0.999, for each month. The amount of the intercept shift varies by month, and is larger in winter than summer. In addition, the difference between the two extracted extents trends downward in all months, as shown in Figure 5.

Figure 2: Extracted Sea Ice Extents and Four Raw Indicators, by Month, λ_S=1

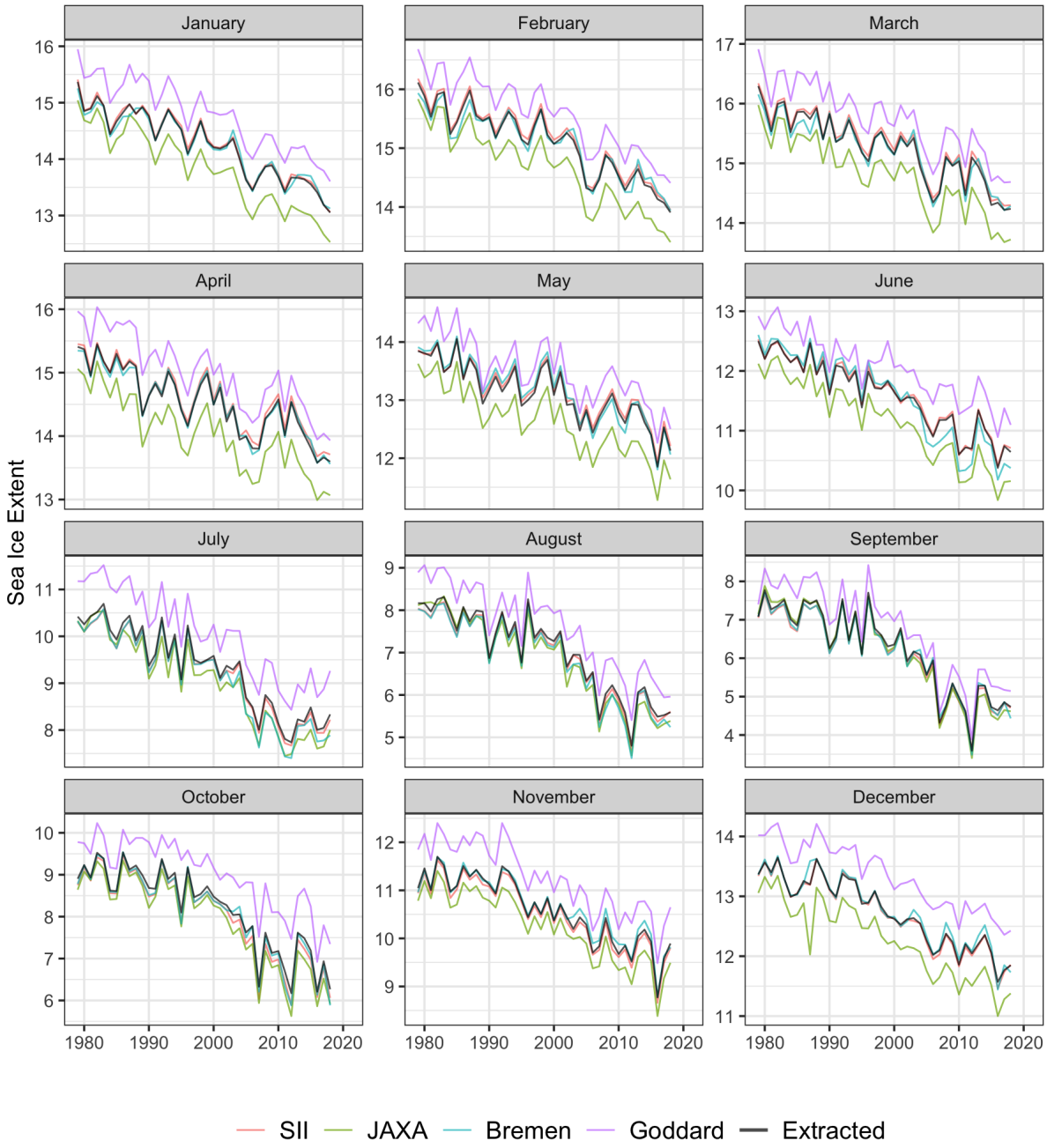

Notes: We show sea ice extent extracted assuming λ_S=1, together with four raw indicators: the Sea Ice Index (SII), Japan Aerospace Exploration agency (JAXA), University of Bremen (Bremen), and Goddard Bootstrap (Goddard). Units are millions of square kilometers.

Figure 3: Extracted Latent Sea Ice Extents and Four Raw Indicators, by Month, λ_G=1

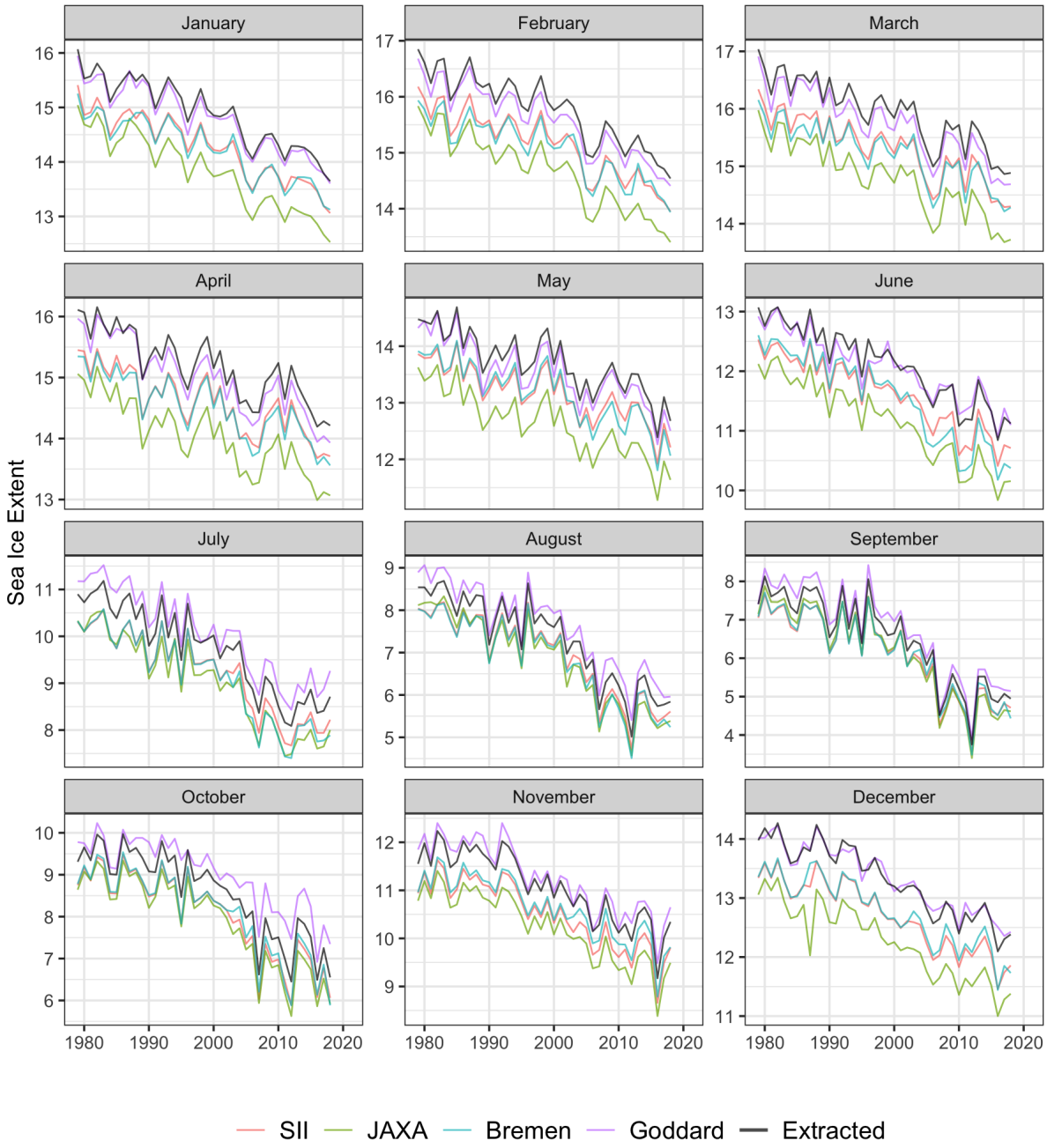

Notes: We show sea ice extent extracted assuming λ_G=1, together with four raw indicators: the Sea Ice Index (SII), Japan Aerospace Exploration agency (JAXA), University of Bremen (Bremen), and Goddard Bootstrap (Goddard). Units are millions of square kilometers.

Because $\widehat{SIE^*}(\lambda_S{=}1)$ and $\widehat{SIE^*}(\lambda_G{=}1)$ are identical up to a linear transformation, it makes no difference which $\widehat{SIE^*}$ we use for research focused on linear *relationships* between SIE^* and other aspects of climate (e.g., various radiative forcings). The obvious choice, then, is $\widehat{SIE^*}(\lambda_S{=}1)$, which is just SIE^S itself, dispensing with the need to estimate the factor model.

4 Summary and Conclusion

We propose a dynamic factor model for several Arctic sea ice extent indicators (Goddard, Sea Ice Index, JAXA, Bremen). We estimate the model and use it in conjunction with the Kalman smoother to produce a statistically-optimal combination of the individual indicators, effectively "averaging out" the individual measurement errors. We explore two identification strategies corresponding to two different factor loading normalizations. The corresponding two extracted combined measures (latent factors) are identical up to a linear transformation, so either one can be used to explore relationships of sea ice extent and other variables. Interestingly, however, the extracted factor for one of the normalizations puts all weight on the Sea Ice Index. Hence the Sea Ice Index alone is a statistically optimal "combination" and one can simply use it alone with no loss, dispensing with the need to estimate the factor model. That is, there is no gain from combining the Sea Ice Index with other indicators, confirming and enhancing confidence in the Sea Ice Index and the NASA Team algorithm on which it is based, and similarly lending credibility – in a competition against very sophisticated opponents – to the NSIDC's claim that the Sea Ice Index is the "final authoritative SMMR, SSM/I, and SSMIS passive microwave sea ice concentration record" (Fetterer et al., 2017).

Figure 4: Extracted Sea Ice Extent, by Month

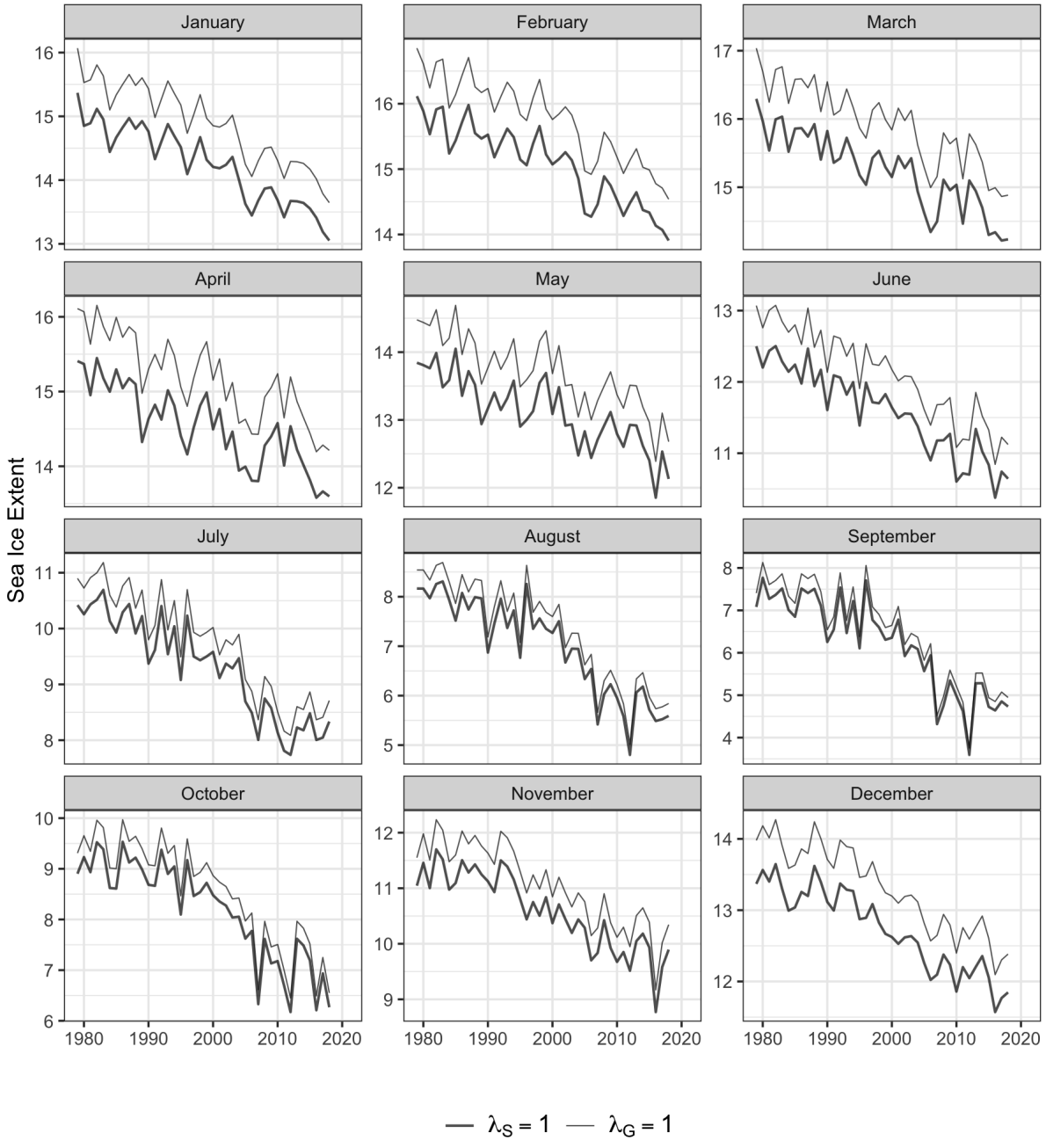

Notes: Units are millions of square kilometers.

Figure 5: Differences in *SIE* Extractions for Different Normalizations (λ_G=1 vs λ_S=1)

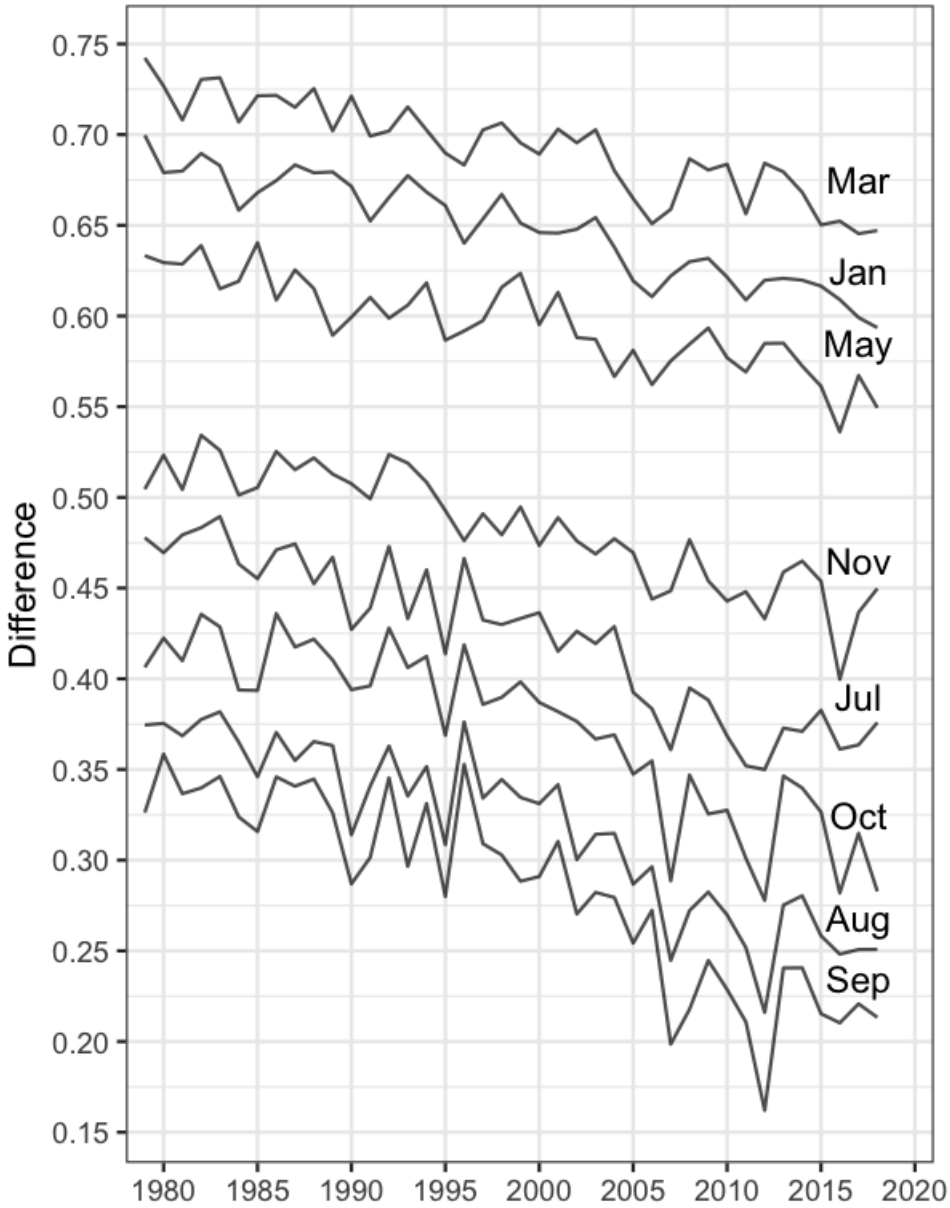

Notes: We show $\widehat{SIE}^*(\lambda_G{=}1) - \widehat{SIE}^*(\lambda_S{=}1)$, for selected months. Units are millions of square kilometers.

References

Aruoba, S.B., F.X. Diebold, J. Nalewaik, F. Schorfheide, and D. Song (2016), "Improving GDP Measurement: A Measurement-Error Perspective," *Journal of Econometrics*, 191, 384–397.

Bunzel, F., D. Notz, J. Baehr, W.A. Müller, and K. Fröhlich (2016), "Seasonal Climate Forecasts Significantly Affected by Observational Uncertainty of Arctic Sea Ice Concentration," *Geophysical Research Letters*, 43, 852–859.

Cavalieri, D.J., C.L. Parkinson, N. DiGirolamo, and A. Ivanoff (2012), "Intersensor Calibration between F13 SSMI and F17 SSMIS for Global Sea Ice Data Records," `https://ntrs.nasa.gov/archive/nasa/casi.ntrs.nasa.gov/20120009376.pdf`, accessed: 2019-08-31.

Cavalieri, D.J., C.L. Parkinson, P. Gloersen, and H.J. Zwally (1996), "Sea Ice Concentrations from Nimbus-7 SMMR and DMSP SSM/I-SSMIS Passive Microwave Data, Version 1," `https://doi.org/10.5067/8GQ8LZQVL0VL`, accessed: 2019-08-29.

Comiso, J.C. (2007), "Enhanced Sea Ice Concentrations from Passive Microwave Data," `https://nsidc.org/sites/nsidc.org/files/files/data/pm/Bootstrap_Algorithm_Revised07.pdf`, accessed: 2019-08-30.

Comiso, J.C. (2017), "Bootstrap Sea Ice Concentrations from Nimbus-7 SMMR and DMSP SSM/I-SSMIS, Version 3," `https://doi.org/10.5067/7Q8HCCWS4I0R`, accessed: 2019-08-29.

Comiso, J.C., D.J. Cavalieri, C.L. Parkinson, and P. Gloersen (1997), "Passive microwave algorithms for sea ice concentration: A comparison of two techniques," *Remote Sensing of Environment*, 60, 357 – 384.

Comiso, J.C., R.A. Gersten, L.V. Stock, G.J. Turner, J.and Perez, and K. Cho (2017b), "Positive Trend in the Antarctic Sea Ice Cover and Associated Changes in Surface Temperature," *Journal of Climate*, 30, 2251–2267.

Comiso, J.C., W.N. Meier, and R. Gersten (2017), "Variability and trends in the Arctic Sea ice cover: Results from different techniques," *Journal of Geophysical Research: Oceans*, 122, 6883–6900.

Diebold, F.X. and G.D. Rudebusch (2019), "Probability Assessments of an Ice-Free Arctic: Comparing Statistical and Climate Model Projections," Working Paper, arXiv:1912.10774 [stat.AP, econ.EM], `https://arxiv.org/abs/1912.10774` .

Fetterer, F., K. Knowles, W.N. Meier, M. Savoie, and A.K. Windnagel (2017), "Sea Ice Index, Version 3," https://doi.org/10.7265/N5K072F8, accessed: 2019-08-29.

Goldstein, M.A, A.H. Lynch, A. Zsom, T. Arbetter, A. Chang, and F. Fetterer (2018), "The Step-Like Evolution of Arctic Open Water," *Nature Scientific Reports*, 8, 16902.

Harvey, A.C. (1989), *Forecasting, Structural Time Series Models, and the Kalman Filter*, Cambridge University Press.

Hillebrand, E., F. Pretis, and T. Proietti (2020), *Econometric Models of Climate Change*, Special Issue of *Journal of Econometrics*, 214, 1-294.

IPCC (2019), *IPCC Special Report on the Ocean and Cryosphere in a Changing Climate* [Pörtner, H.-O. and Roberts, D.C. and Masson-Delmotte, V. and Zhai, P. and Tignor, M. and Poloczanska, E. and Mintenbeck, K. and Nicolai, M. and Okem, A. and Petzold, J. and Rama, B. and Weyer, N. (eds.)], https://www.ipcc.ch/srocc/.

Ivanova, N., L.T. Pedersen, R.T. Tonboe, S. Kern, G. Heygster, T. Lavergne, A. Sørensen, R. Saldo, G. Dybkjær, L. Brucker, and M. Shokr (2015), "Inter-Comparison and Evaluation of Sea Ice Algorithms: Towards Further Identification of Challenges and Optimal Approach Using Passive Microwave Observations," *The Cryosphere*, 9, 1797–1817.

Maslanik, J. and J. Stroeve (1999), "Near-Real-Time DMSP SSMIS Daily Polar Gridded Sea Ice Concentrations, Version 1," https://doi.org/10.5067/U8C09DWVX9LM, accessed: 2019-08-29.

Meier, W.N., G. Peng, D.J. Scott, and M.H. Savoie (2014), "Verification of a new NOAA/NSIDC Passive Microwave Aea-Ice Concentration Climate Record," *Polar Research*, 33, 21004.

Meier, W.N. and J.S. Stewart (2019), "Assessing Uncertainties in Sea Ice Extent Climate Indicators," *Environmental Research Letters*, 14, 035005.

Parkinson, C.L. and D.J. Cavalieri (2008), "Arctic Sea Ice Variability and Trends, 1979-2006," *Journal of Geophysical Research: Oceans*, 113.

Peng, G., W.N. Meier, D.J. Scott, and M.H. Savoie (2013), "A Long-Term and Reproducible Passive Microwave Sea Ice Concentration Data Record for Climate Studies and Monitoring," *Earth System Science Data*, 5, 311–318.

Spreen, G., L. Kaleschke, and G. Heygster (2008), "Sea ice remote sensing using AMSR-E 89-GHz channels," *Journal of Geophysical Research: Oceans*, 113.